Effects of doping with magnetic cations on the hybrid improper ferroelectricity in $Sr_3Sn_2O_7$

J. Blasco [a,b,*], D. Gracia [a,b], S. Lafuerza [a,b], V. Cuartero [a,c], G. Subías [a,b]

[a] Instituto de Nanociencia y Materiales de Aragón (INMA), CSIC-Universidad de Zaragoza, Zaragoza 50009, Spain
[b] Departamento de Física de la Materia Condensada, Universidad de Zaragoza, C/ Pedro Cerbuna 12, Zaragoza 50009, Spain
[c] Departamento de Ciencia y Tecnología de Materiales y Fluidos, EINA, Universidad de Zaragoza, C/María de Luna 3, Zaragoza 50018, Spain

ARTICLE INFO

ABSTRACT

We here report the structural, magnetic and electrical properties of $Sr_{2.9}La_{0.1}Sn_{1.9}M_{0.1}O_7$ (M= Cr, Mn or Fe) compounds. This La/M codoping of the hybrid improper ferroelectric $Sr_3Sn_2O_7$, allows introducing magnetic cations into the perovskite layers of this Ruddlesden-Popper phase. The doping induces minor structural changes, preserving the polar structure with space group $A2_1am$ of the undoped compound. The perovskite tolerance factor of all doped samples is slightly lower than in $Sr_3Sn_2O_7$, which preserves the tilts and rotations of SnO_6 octahedra. Doped samples exhibit a paramagnetic behavior down to 5 K and obey the Curie-Weiss law above 200 K. The effective paramagnetic moments agree with the expected spin-only values of the respective magnetic M^{3+} cations. All samples show a ferroelectric hysteresis loop at room temperature, but the doped samples show larger coercive fields. Additionally, the doping with magnetic cations has important effects on the dielectric properties: a strong decrease of the temperature of the ferroelectric transition together with a smoothing of the anomaly in the dielectric permittivity. These results suggest that the disorder produced by the two aliovalent substitutions is detrimental for the ferroelectric properties due to point charge defects but, at the same time, the prevalence of the structural distortion (tilts and rotations) preserves the ferroelectricity in the investigated doping regime.

1. Introduction

Over the past decades, magnetoelectric multiferroics have attracted a large interest due to promising technological applications in data storage, spintronics or wireless energy transfer [1–3]. Despite this motivation, it remains a great challenge to find functional multiferroic materials which operate at room temperature. The reason is that, in most cases, the conditions for ferroelectricity and magnetic ordering hamper each other [4]. On one side, the most common ferroelectric compounds adopt an ABO₃ perovskite (or related) type structure and the distortion leading to the spatial inversion symmetry breaking is favored by atoms with an empty *d* shell. Meanwhile, long-range magnetic ordering requires transition metals with partially filled *d* orbitals. In order to overcome this contraindication, many alternatives have been sought, including mechanisms where ferroelectricity is induced by incommensurate magnetism, charge ordering or geometric mechanisms [1,2,5–7]. Concerning the latter, the hybrid improper ferroelectric (HIF) mechanism is recently drawing attention [8,9] since it gives rise to ferroelectric

behavior at room temperature. This mechanism is fully operational in layered perovskite structures such as Ruddlesden-Popper (RP), Dion-Jacobson or Aurivillius phases. It consists of the coupling between two main non-polar distortions (associated with tilts and rotations of the BO₆ octahedra) that favor the condensation of a secondary ferroelectric distortion [8–10]. The striking aspect of this trilinear coupling is that it is not induced by conventional d^0 cation displacements, being a priori compatible with the presence of d^n magnetic cations at the B site of the perovskite layers.

Recently, it has been shown that $Sr_3Sn_2O_7$ is a HIF system with switchable electric polarization at room temperature, and a large coercive field in polycrystalline samples [11,12]. This compound (see Fig. 1) belongs to the family of RP phases with two perovskite layers ($SrSnO_3$) separated by a rock salt layer (SrO) along the *c* axis. Also, it has been successfully grown as single crystals exhibiting a smaller coercive field with respect to the ceramic specimens [13]. The replacement of strontium with other alkaline earth metals (A= Ba, Ca) increases the Curie temperature (Tc) as the size of the A atom decreases [14,15]. Similar
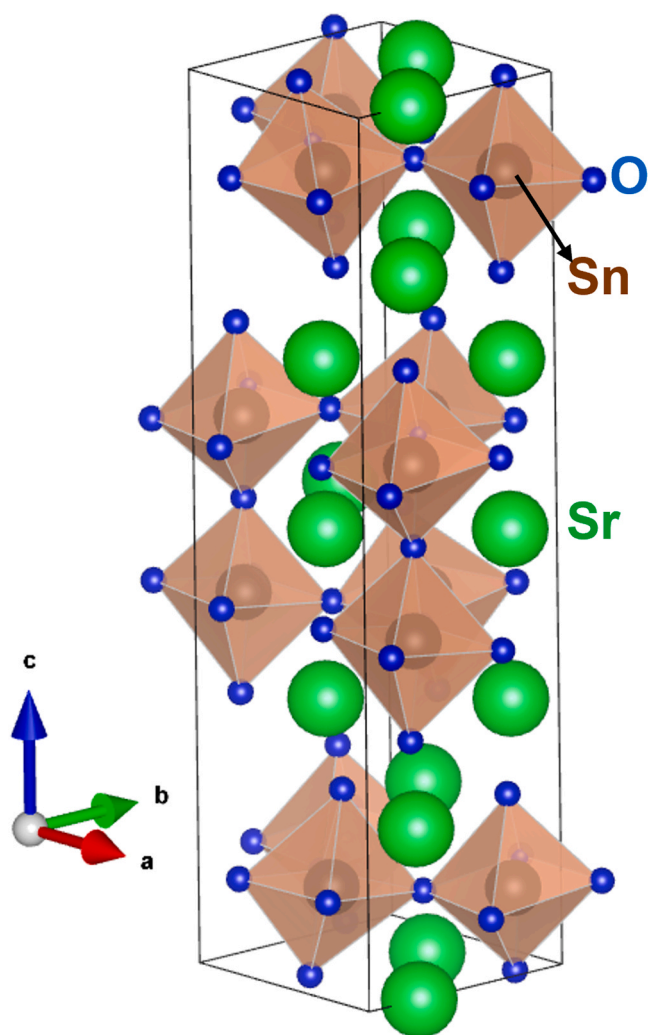

Fig. 1. Orthorhombic crystal structure (*A2$_1$am* space group) of Sr$_3$Sn$_2$O$_7$ at room temperature.

results have been reported in related HIF compounds [16,17], suggesting a linear relationship between T$_C$ and the tolerance factor (*t*-factor) of the perovskite layers defined as $t=(r_A+r_O)/\sqrt{2}(r_B-r_O)$, where r$_A$, r$_B$ and r$_O$ represent the ionic radii of A-site cation, B-site cation, and oxygen anion, respectively. Consequently, a decrease of *t*-factor favors the tilts and rotations of the SnO$_6$ octahedra, that lead to the appearance of HIF behavior. We note that, however, the large ferroelectric polarization observed in Ba-doped compounds is ascribed to the combined effect of a tilt increase and a rotation decrease that cannot be directly inferred from the evolution of *t*-factor [14].

The identification of HIF behavior in Sr$_3$Sn$_2$O$_7$ makes it very attractive for developing new multiferroics by replacing Sn with magnetic cations. To our knowledge, this type of substitution has not been explored so far. Therefore, the initial step is to determine if it is possible to incorporate magnetic cations in the Sn sublattice while preserving the ferroelectric properties of the parent compound. Previous studies on the related RP phase Ca$_3$Ti$_2$O$_7$ have reported that the partial replacement of Ti by Co as an acceptor dopant results in the appearance of oxygen vacancies. This leads to leakage effects on the dielectric properties of the ceramic specimens [18], which are detrimental for ferroelectricity. Meanwhile, the use of small amounts of Nd^{3+} as donor dopant in Ca$_3$Ti$_2$O$_7$ was reported to be an effective way to decrease oxygen vacancies, leading to improved ferroelectric properties [19]. Consequently, simultaneous substitution at both A and B crystallographic sites may be a suitable strategy to incorporate magnetic cations in HIF

compounds without weakening their ferroelectric properties. In this context, we have thoroughly investigated the effects of doping the Sn sublattice in Sr$_3$Sn$_2$O$_7$ with three different types of magnetic atoms (M=Cr, Fe and Mn). Since these magnetic cations are formally trivalent and they are replacing Sn^{4+} (acceptor dopants), a simultaneous substitution of Sr^{2+} with La^{3+} (donor dopant) is incorporated to preserve the charge balance. Therefore, this work focuses on the synthesis of Sr$_{2.9}$La$_{0.1}$Sn$_{1.9}$M$_{0.1}$O$_7$ compounds with M= Cr, Fe or Mn and the resultant structural, magnetic and electrical properties, relative to the non-magnetic HIF counterpart Sr$_3$Sn$_2$O$_7$.

2. Experimental details

Polycrystalline samples of Sr$_3$Sn$_2$O$_7$ and Sr$_{2.9}$La$_{0.1}$Sn$_{1.9}$M$_{0.1}$O$_7$ (M=Cr, Fe or Mn) were synthesized by solid state reaction in three steps. Stoichiometric amounts of SnO$_2$, SrCO$_3$ and M$_2$O$_3$ were mixed, ground and heated at 1000° C for 15 h in air. The resulting powder was reground, pressed into pellets and sintered at 1300° C for 24 h. The pellets were reground, repressed and sintered at 1400° C for another 24 h. The heating and cooling ramps were 5°C/min in all steps. Density measurements on the resulting pellets were performed using the Archimedes' method, obtaining relative densities between 91 % and 93 %. The samples were characterized by X-ray powder diffraction (XRD) using a Rigaku D/MAX 2500-system and Cu Kα$_{1,2}$ wavelengths. Rietveld analysis of the XRD patterns were performed with the Fullprof program [20]. The Rigaku accessory for temperature-dependent diffraction measurements from –180°C to 300°C in vacuum was installed to collect diffraction patterns between 40° and 225° C. The chemical composition of the samples was analyzed by wavelength dispersive X-ray fluorescence spectrometry (advant'XP+ model manufactured by ARL). The Sr:Sn:M ratio agreed with the nominal one for all samples. The schematic illustrations of the crystal structures were performed with the VESTA program [21].

Room temperature X-ray absorption spectroscopy (XAS) measurements at the Mn K edge were performed at beamline BM23 of the ESRF (The European Synchrotron) [22] for Sr$_{2.9}$La$_{0.1}$Sn$_{1.9}$Mn$_{0.1}$O$_7$ and the reference compounds CaMnO$_3$, LaMnO$_3$ and Ca$_3$Mn$_2$O$_7$. Pellets of the reference compounds were prepared by dilution with cellulose to get a jump of about 1 at the absorption edge and they were measured in transmission mode. Due to the low Mn content, XAS measurements on Sr$_{2.9}$La$_{0.1}$Sn$_{1.9}$Mn$_{0.1}$O$_7$ were conducted in fluorescence mode instead, using a Hitachi Vortex Si drift detector. The spectra were normalized and compared using the program Athena from the Demeter package [23].

Magnetic measurements were carried out between 5 and 320 K by using a commercial Superconducting Quantum Interference Device (SQUID, Quantum Design). Electrical properties measurements were conducted on sintered disc-shaped samples, with typical dimensions of 8 mm diameter and thicknesses from 0.2 to 0.7 mm. Electrodes were made with silver paste in sandwich geometry. The relative dielectric permittivity was derived from measurements with an impedance analyzer (Wayne Kerr Electronics 6500B), applying sinusoidal excitations of 1 V amplitude at 900 kHz. Temperature dependent measurements were conducted in a homemade sample insert placed inside a tubular furnace. Both heating and cooling ramps with a typical velocity value of 1 K/minute were applied. The polarization versus electric field (*P-E*) hysteresis loops were collected at room temperature in silicon oil, using a 500 V-built-in ferroelectric tester (Precision Premier II, Radiant Technologies) jointly with a high voltage amplifier (610E, Trek). We used two different measurement protocols, the standard bipolar triangular voltage pulse and the remanent hysteresis measurement to identify the intrinsic ferroelectric polarization [24,25]. Excitation signals with frequency of 250 Hz and maximum electric (*E*) field amplitude between 100 and 225 kV/cm, depending on the sample, were applied.

3. Results and discussion

3.1. Structural characterization

The XRD patterns of the $Sr_{3-x}La_xSn_{2-x}M_xO_7$ (x=0 and 0.1; M=Cr, Fe or Mn) compounds confirm that they are single phase and agree with a bilayered RP phase adopting an orthorhombic unit cell (see Fig. S1 in the supplementary information). Accurate Rietveld refinements can be obtained for all compounds as can be seen in Fig. 2 for $Sr_{2.9}La_{0.1}Sn_{1.9}Mn_{0.1}O_7$ and for the rest of the samples in the supplementary information (Fig. S2-S4). The refined structural parameters are summarized in Table 1. The values for $Sr_3Sn_2O_7$ are in accordance with previous reports [12] and agree with the polar orthorhombic $A2_1am$ space group. The other three samples are isostructural to $Sr_3Sn_2O_7$ and exhibit smaller unit cells, which can be attributed to the smaller sizes of the incorporated atoms. The radius of La^{3+} (r_{La}^{3+}) is smaller than that of Sr^{2+} (r_{Sr}^{2+}) and, according to tabulated data, $r_{Sn}^{4+} > r_{Fe}^{3+} = r_{Mn}^{3+} > r_{Cr}^{3+}$ [26]. In this way, the smallest unit cell corresponds to the Cr-doped compound as anticipated by the tabulated radii. At the same time, we find that the Mn-doped compound has an unexpectedly smaller unit cell volume than the Fe-doped. A detailed inspection to the lattice parameters reveals that the most significant anomaly is a larger contraction of the *c* axis for the Mn-doped compound. A possible explanation for this deviation would be a partial oxidation of Mn. To investigate this, we have carried out XAS measurements at the Mn K-edge. A linear chemical shift of 4.3 eV at this edge between Mn^{3+} ($LaMnO_3$) and Mn^{4+} ($CaMnO_3$) is observed in the $La_{1-x}Ca_xMnO_3$ series [27] and has been used to evaluate the chemical valence of Mn in different manganites [28]. The XAS spectrum of $Sr_{2.9}La_{0.1}Sn_{1.9}Mn_{0.1}O_7$ shows an energy position of the absorption edge much closer to the Mn^{3+} reference than to the Mn^{4+} compounds ($CaMnO_3$ or $Ca_3Mn_2O_7$) as can be seen in the Fig. S5 (supplementary information). Therefore, the chemical valence of Mn in $Sr_{2.9}La_{0.1}Sn_{1.9}Mn_{0.1}O_7$ is close to +3. In addition, the XAS spectrum for $Sr_{2.9}La_{0.1}Sn_{1.9}Mn_{0.1}O_7$ exhibits pre-edge features very similar to those shown in the $LaMnO_3$ spectrum indicating similar 1 s→3d transitions in both compounds and similar Mn *3d* holes for both samples. Furthermore,

Table 1

Refined lattice parameters, tolerance factor, fractional atomic coordinates, isotropic temperature factors and reliability factors for $Sr_3Sn_2O_7$ and $Sr_{2.9}La_{0.1}Sn_{2.9}M_{0.1}O_7$ (M=Cr, Mn or Fe).

	$Sr_3Sn_2O_7$	M=Cr	M=Mn	M=Fe
a (Å)	5.7066(1)	5.6985(1)	5.7019(1)	5.7016(1)
b (Å)	5.7352(1)	5.7269(1)	5.7308(1)	5.7296(1)
c (Å)	20.6649(1)	20.6320(2)	20.6127(2)	20.6365(1)
Vol. (Å³)	676.33(1)	673.32(1)	20.6127(2)	674.15(1)
t-factor	0.953(4)	0.945(5)	0.938(5)	0.949(4)
Sr1(La): x	0.0240(7)	−0.0232(8)	−0.0178(9)	−0.0244(8)
y	0.2477(9)	0.2466(9)	0.2477(9)	0.2436(9)
B (Å²)	0.13(6)	0.42(6)	0.69(5)	0.27(7)
Sr2: x	0.0025(6)	−0.0000(7)	0.0030(7)	0.0002(7)
y	0.7399(5)	0.7394(6)	0.7400(5)	0.7403(6)
z	0.31223(5)	0.31258(6)	0.31254(5)	0.31180(6)
B (Å²)	0.30(4)	0.33(4)	0.52(4)	0.12(5)
Sn(M): x	0.0	0.0	0.0	0.0
y	0.7498(5)	0.7500(5)	0.7492(4)	0.7502(5)
z	0.09830(6)	0.09855(7)	0.09847(6)	0.09853(8)
B (Å²)	0.31(3)	0.43(3)	0.37(2)	0.54(3)
O1: x	−0.003(6)	0.010(8)	0.005(8)	−0.010(7)
y	0.707(4)	0.708(5)	0.699(3)	0.717(6)
B (Å²)	0.89(19)	0.83(19)	0.64(16)	1.0(2)
O2: x	−0.016(4)	−0.008(6)	−0.009(5)	−0.016(5)
y	0.784(3)	0.788(3)	0.785(3)	0.789(3)
z	0.1979(4)	0.1993(5)	0.1965(3)	0.2040(6)
B (Å²)	0.89(19)	0.83(19)	0.64(16)	1.0(2)
O3a: x	0.272(3)	0.239(4)	0.240(4)	0.239(4)
y	−0.034(3)	0.016(4)	−0.006(4)	0.016(4)
z	0.0857(5)	0.0880(5)	0.0881(4)	0.0880(5)
B (Å²)	0.18(19)	0.54(19)	0.68(17)	0.12(19)
O3b: x	0.732(3)	0.781(4)	0.777(4)	0.236(4)
y	0.513(3)	0.460(4)	0.460(4)	0.035(4)
z	0.1102(5)	0.1100(5)	0.1094(4)	0.0862(6)
B (Å²)	0.18(19)	0.54(19)	0.68(17)	0.12(19)
R_{exp} (%)	5.3	5.4	5.2	5.4
R_{Bragg} (%)	3.7	4.4	2.2	4.35
χ^2	2.35	2.2	1.7	2.5

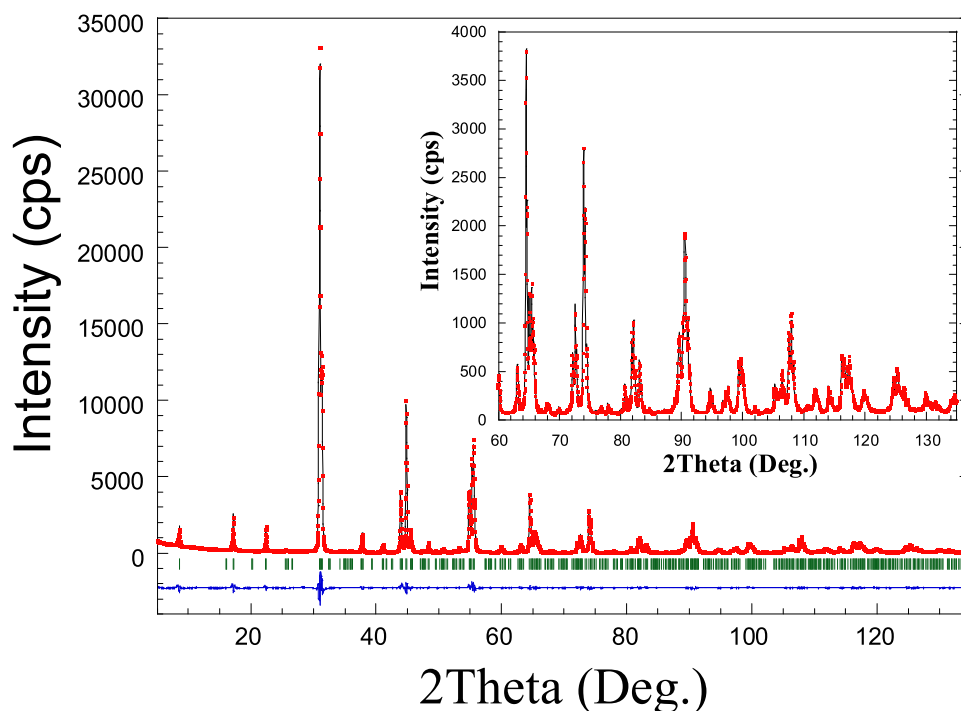**Fig. 2.** Observed (points), calculated (full line) and difference (bottom) x-ray diffraction profiles for $Sr_{2.9}La_{0.1}Sn_{1.9}Mn_{0.1}O_7$. The bars indicate the allowed reflections. Inset: Detail of the same refinement at high angles.

the small chemical shift (0.5 eV) between the edges of these two formal Mn^{3+} compounds can be ascribed to the difference between the Jahn-Teller (JT) Mn^{3+} in $LaMnO_3$ and the non-JT Mn^{3+} in $Sr_{2.9}La_{0.1}Sn_{1.9}Mn_{0.1}O_7$, as previously observed in related systems [29]. The non-JT Mn^{3+} is forced by its dilution in a rigid matrix (d^{10} cations as Ga^{3+} or Sn^{4+}) that prevents this type of distortions. Accordingly, a possible explanation for slight discrepancy of structural data in the Mn-doped sample (see Table 1) may be ascribed to the occurrence of non-JT Mn^{3+} in this compound, whose ionic radius might deviate from the tabulated one, usually calculated from JT Mn^{3+}.

We have also calculated the *t*-factor from the refined structural data and we have found similar values for all samples (within experimental errors) although the Mn-doped sample deviates slightly from this trend. In any case, all doped compounds seem to exhibit similar (within error bars) or even smaller *t*-factor than the undoped sample, which should preserve the rotations and tilts of the $Sn(M)O_6$ octahedra observed in the parent compound.

Fig. 3 shows the temperature dependence of the lattice parameters for the four samples. The ferroelectric transition gives rise to clear anomalies in the evolution of the three crystallographic axes of $Sr_3Sn_2O_7$, which follow an anisotropic behavior in agreement with previous results [12]. That is, while the *a* and *b* axes undergo a sudden contraction at $T_C \approx 130°$ C upon heating (see Fig. 3a-b), the *c* axis exhibits a coupled expansion (see Fig. 3c). Accordingly, this transition is barely noticeable in the temperature dependence of the unit cell volume as can be seen in Fig. 3d. Similar effects are observed in the three doped

samples, but the anomalies are considerably weaker and occur at lower temperatures, with similar values around $T_C \approx 70-80°$ C. Although this result seems to contradict the linear relationship reported between T_C and *t*-factor for HIF compounds [17], we note that there are additional effects that must be taken into account. Recent calculations have revealed a strong competition between the rotation of the BO_6 octahedra (causing the HIF mechanism) and an atomic rumpling at the rock salt-perovskite interface producing a deformation of the BO_6 octahedra [30]. The presence of trivalent cations (like La^{3+}) in the rock salt layer seems to favor this atomic rumpling. At the same time, some studies on related systems have revealed that disordering of Sr^{2+}/La^{3+} cations on perovskite and rock-salt sites suppresses the rumpling-induced octahedral deformation preserving BO_6 rotations [31]. Finally, another important aspect to consider is that the relationship between T_C and *t*-factor has been obtained in compounds with the B sublattice free of defects. In our samples, atom replacements are produced in both, A- and B-sites and this disorder may affect the coherence of BO_6 rotations, weakening the HIF mechanism.

3.2. Magnetic properties

The magnetization curves M(T) were measured for the three doped samples. As expected for these small substitutions, they exhibit a paramagnetic behavior in the whole temperature range. Fig. 4(a) shows the temperature dependence of the inverse of the magnetic susceptibility after diamagnetic correction using tabulated data and the additive
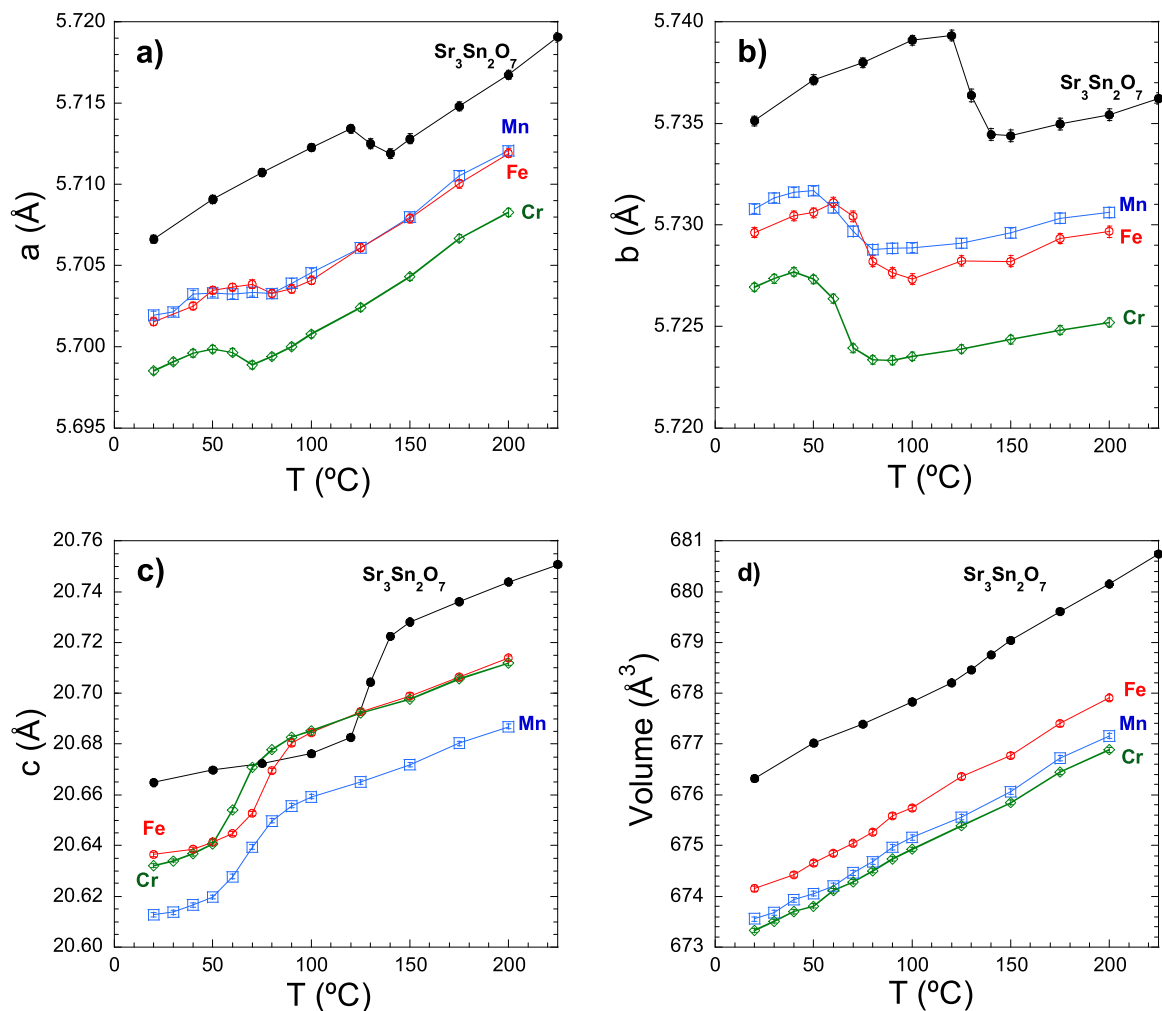

Fig. 3. Temperature dependence of the lattice parameters (a, b and c) and unit cell volume (d) for $Sr_3Sn_2O_7$, $Sr_{2.9}La_{0.1}Sn_{1.9}Cr_{0.1}O_7$ (Cr), $Sr_{2.9}La_{0.1}Sn_{1.9}Mn_{0.1}O_7$ (Mn) and $Sr_{2.9}La_{0.1}Sn_{1.9}Fe_{0.1}O_7$ (Fe).
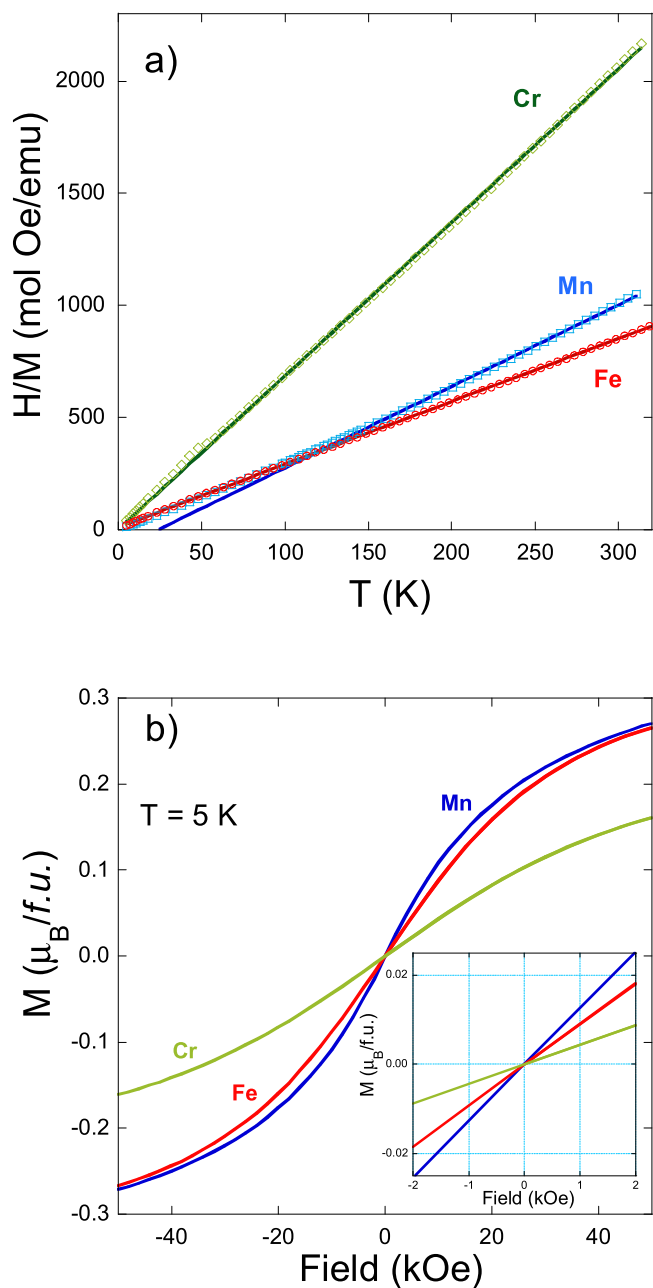
Fig. 4. (a) The inverse magnetic susceptibility versus temperature for $Sr_{2.9}La_{0.1}Sn_{1.9}Cr_{0.1}O_7$ (Cr), $Sr_{2.9}La_{0.1}Sn_{1.9}Mn_{0.1}O_7$ (Mn) and $Sr_{2.9}La_{0.1}Sn_{1.9}Fe_{0.1}O_7$ (Fe). The solid lines are fits to the Curie-Weiss law. (b) Isothermal magnetization measurements for the same samples at 5 K. Inset: Detail of the same curves at low magnetic fields.

Table 2

Curie constant (C), Weiss constant (θ) and experimental effective paramagnetic moments (ρ_{eff}) obtained from the fit to a Curie-Weiss law. Theoretical effective paramagnetic moments (ρ_{theo}) have been calculated from experimental values for spin-only contribution of Cr^{3+}, high-spin Mn^{3+} and high-spin Fe^{3+}.

Sample	C (emu/K mol)	θ (K)	ρ_{eff} (μ_B/fu)	ρ_{theo} (μ_B/fu)	Fit Range
$Sr_{2.9}La_{0.1}Sn_{1.9}Cr_{0.1}O_7$	0.145	−6	1.08	1.20	50–310 K
$Sr_{2.9}La_{0.1}Sn_{1.9}Mn_{0.1}O_7$	0.27	311	1.47	1.55	150–310 K
$Sr_{2.9}La_{0.1}Sn_{1.9}Fe_{0.1}O_7$	0.355	−33.5	1.69	1.86	10–320 K

approximation [32]. The Fe- and Cr- doped samples exhibit an almost linear behavior in the whole temperature range. These samples obey the Curie-Weiss law given by: $\chi = C/(T-\theta)$, where C is the Curie constant and θ is the Weiss constant. Table 2 summarizes the magnetic parameters obtained from the linear fits shown in Fig. 4(a). These parameters reasonably agree with the expected spin-only contribution from the magnetic cations. The calculated effective paramagnetic moments (ρ_{eff}) are slightly smaller than the theoretical ones (see Table 2), which may indicate the existence of magnetic correlations in the paramagnetic phase. The values of the Weiss constants are very small for Cr- and Fe-doped samples revealing weak interactions. Their negative values suggest antiferromagnetic correlations, in agreement with the expected interactions according to the Goodenough-Kanamori rules for super-exchange interactions [33,34]. On the other hand, a deviation from the linear behavior is observed in the measurement of Mn-doped sample, suggesting stronger magnetic correlations. Reasonable fits to a Curie-Weiss law can be obtained above 150 K. The ρ_{eff} values are in accordance with the spin-only contribution of high-spin Mn^{3+} atoms but the high value of the Weiss Constant seems somewhat unphysical (see Table 2). In any case, its positive sign suggests the presence of ferro-magnetic correlations in this sample. This result may be understood within the framework of the magnetic properties observed in simple perovskites when non-JT Mn^{3+} cations are diluted in a non-magnetic matrix (like $LaGa_{1-x}Mn_xO_3$ or $LaSc_{1-x}Mn_xO_3$). These compounds do not follow the Goodenough-Kanamori rules and even some compositions (x∼ 0.5) exhibit a long-range ferromagnetic ordering at low temperature [29,35,36]. In order to evaluate the magnetic ground state of the doped compounds, isothermal magnetization between −50 and −50 kOe were measured at 5 K as can be seen in Fig. 4(b). The three samples show a linear behavior at low magnetic fields without any sign of spontaneous magnetization. This means that all three samples are paramagnetic even at 5 K, in agreement with the low concentration of magnetic ions in the doped samples. The M(H) curves cease to be linear at high magnetic fields, approaching the shape of a Langevin function typical of para-magnetic compounds, without reaching magnetic saturation at 50 kOe.

3.3. Ferroelectric properties

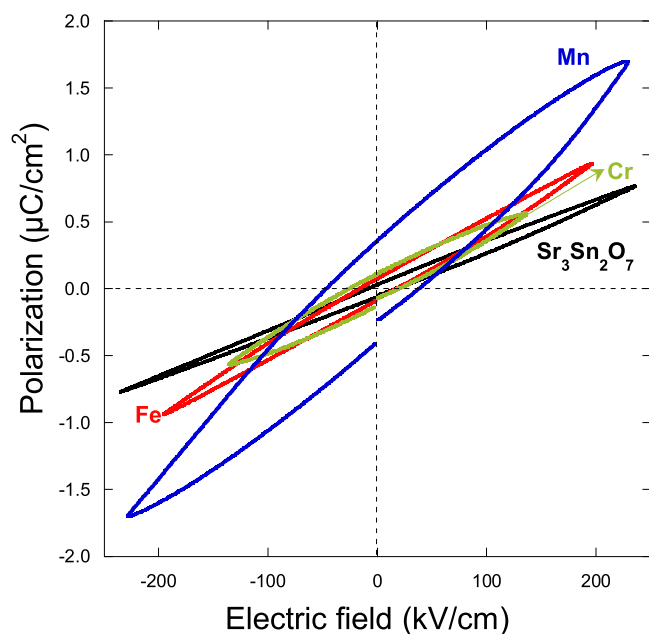To evaluate the ferroelectric properties of codoped

Fig. 5. Polarization hysteresis loops for Sr_3Sn_2O and $Sr_{2.9}La_{0.1}Sn_{1.9}M_{0.1}O_7$ (M= Cr, Fe, Mn) measured at room temperature and at 100 Hz.

$Sr_{2.9}La_{0.1}Sn_{1.9}M_{0.1}O_7$ (M=Cr, Fe, Mn), P-E loops were measured applying the standard bipolar triangular voltage pulse and also the remanent hysteresis measurement protocols [25]. Fig. 5 shows the *P-E* results obtained at the highest E field value allowed by each sample, being the Cr-doped sample the one showing the smallest dielectric breakdown field. The loop for Mn-doped sample exhibits the largest contribution from leakage currents while the other three samples display a similar behavior with a main contribution coming from linear capacitance. In order to gain insights into polarization components, the remanent hysteresis measurement protocol was carried out. This protocol allows getting the remanent polarization by subtracting the non-remanent components, i.e., leakage and linear capacitance contributions [25]. Details on how this measurement protocol works can be consulted in the supplementary material using the Fe-doped sample as representative example (Fig. S6).

Fig. 6 shows the remanent polarization loops of $Sr_{3-x}La_xSn_{2-x}M_xO_7$ (x=0 and 0.1; M=Cr, Fe or Mn) ceramics measured at a frequency of 250 Hz at room temperature at the maximum E field amplitude (E_0) achieved for each sample. The same figure shows the current vs. E field curves where clear peaks around the coercive field (E_C) values of the P-E loops are observed. The well-developed hysteresis loops together with the peaks in the I-E curves demonstrate the presence of intrinsic remanent polarization (P_r) at room temperature for all the measured samples. The P_r value for undoped $Sr_3Sn_2O_7$ and $Sr_{2.9}La_{0.1}Sn_{1.9}Fe_{0.1}O_7$ samples is around 0.04 μC/cm² for E_0 up to about 200 kV/cm, which agrees well with previous reports on the parent compound, considering that E_0 values above 300 kV/cm were applied in those cases [11,12]. At the same time, a similar P_r value is found for the Mn-doped sample (i.e., ~ 0.05 μC/cm² at a slightly larger E_0 of ~230 kV/cm). Regrettably, we could not obtain *P-E* loops at E_0 higher than 160 kV/cm for the $Sr_{2.9}La_{0.1}Sn_{1.9}Cr_{0.1}O_7$ sample (Fid. 6d), because of the limitation by its relatively small breakdown field, but P_r at this field is similar to the value obtained for the Mn-doped sample. On the other hand, the E_C

values of all codoped samples are higher than those of undoped $Sr_3Sn_2O_7$ (see Fig. S7 in the supplementary section) independently of the field-amplitude. These results indicate that the main effect in the ferroelectric properties upon the aliovalent codoping with La^{3+} and magnetic M^{3+} cations, is a hardening the ferroelectric hysteresis loop of
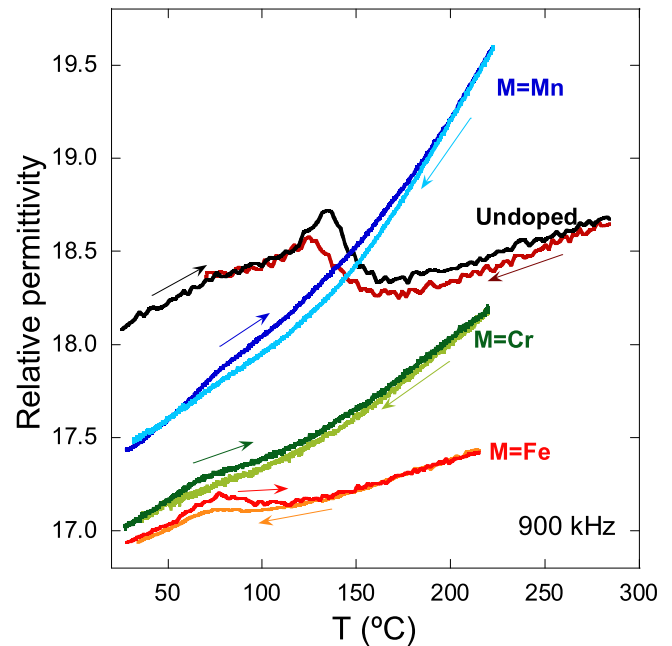

Fig. 7. The real component of the relative dielectric permittivity for $Sr_3Sn_2O_7$, and doped $Sr_{2.9}La_{0.1}Sn_{1.9}M_{0.1}O_7$ (M=Cr, Mn or Fe) samples.
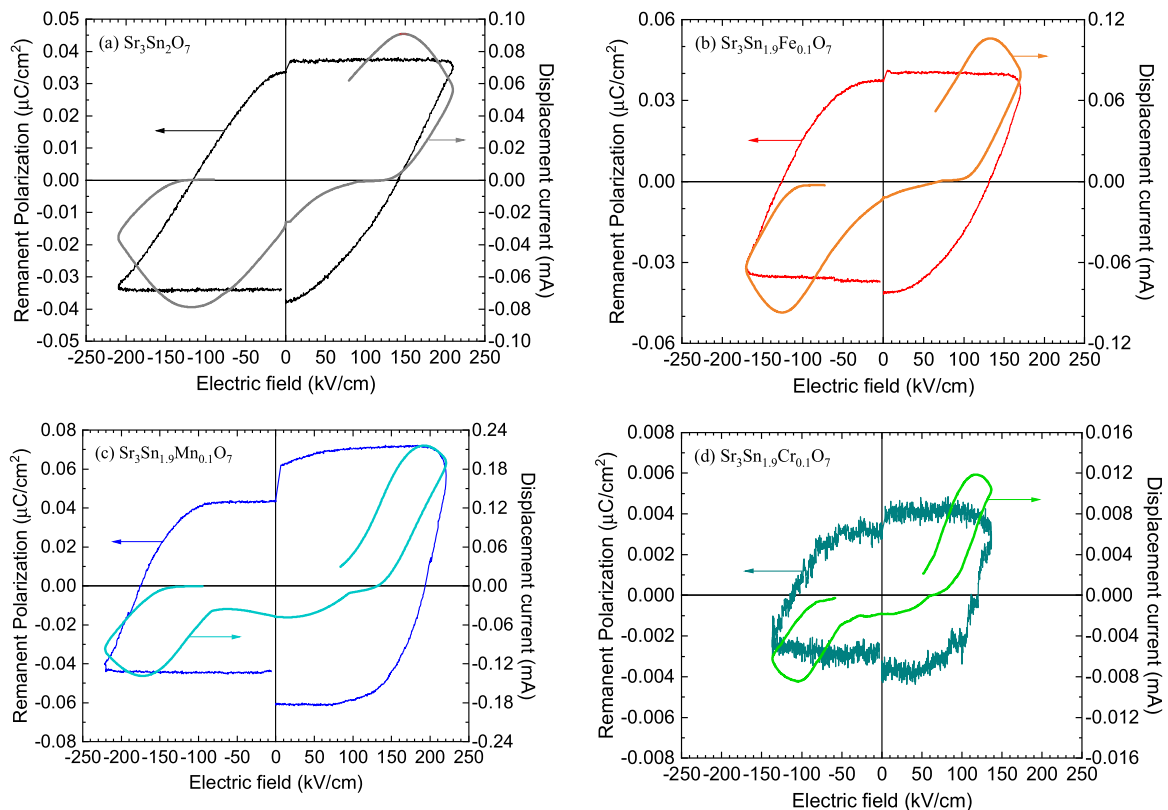

Fig. 6. Remanent Polarization (dark colors) and current (light colors) versus E field curves for (a) $Sr_3Sn_2O_7$, (b) $Sr_{2.9}La_{0.1}Sn_{1.9}Fe_{0.1}O_7$, (c) $Sr_{2.9}La_{0.1}Sn_{1.9}Mn_{0.1}O_7$ and (d) $Sr_{2.9}La_{0.1}Sn_{1.9}Cr_{0.1}O_7$ measured at room temperature and at 250 Hz.

the HIF $Sr_3Sn_2O_7$.

The temperature dependence of the real part of the relative dielectric permittivity for all samples measured at a frequency of 900 kHz is compared in Fig. 7. The ferroelectric transition of $Sr_3Sn_2O_7$ is characterized by an anomaly with a lambda-shape. The peak of the anomaly is at 136° C while the transition onset on the high temperature side is at 160° C. These values agree with previous reports [12,14]. The significant thermal hysteresis between the heating and cooling ramps suggests a first-order transition. Regarding the codoped samples, the transition becomes much smoother, especially in the Cr- and Mn-doped samples in this order. In the case of the Fe-doped sample, a small and broad peak is well noticeable at 77° C. The temperature ranges for the transitions observed in the dielectric permittivity are in reasonable agreement with the anomalies observed in the lattice parameters (compare Figs. 3 and 7). These results indicate that this aliovalent codoping is detrimental for the ferroelectric properties of $Sr_3Sn_2O_7$ despite the small structural changes induced (see Fig. 2) and the decrease in the t-factor (see Table 1). Therefore, the ferroelectric mechanism in these RP-phases depends not only on geometric factors like the t-factor but also on the type of substitution and the induced disorder. Previous studies, focused on isovalent substitutions, found a close correlation between T_C and t-factor [15,34] conditioned by the rumpling distortion of BO_6 octahedra [30,31]. Our study, focused on the doping with magnetic cations, involves a double aliovalent substitution at both sites (Sr and Sn) of the perovskite layers. Thus, we think that the compositional disorder affects the internal E field experienced by dipoles, weakening its ferroelectric arrangement. This results in smaller ordered domains that give rise to more diffuse transitions. A similar effect of aliovalent substitutions in ferroelectric $BaTiO_3$ has also been reported [37]. In that work, the authors show how charge point defects break down the ferroelectric domains into polar clusters.

4. Conclusions

Hybrid improper ferroelectric $Sr_3Sn_2O_7$ can be successfully doped with magnetic cations using a codoping strategy that combines A-site doping (Sr^{2+} replaced by La^{3+}) and B-site doping (Sn^{4+} substituted with Cr^{3+}, Mn^{3+} or Fe^{3+}). For this small substitution (x=0.1), the polar crystal structure is preserved (space group $A2_1am$) but in spite of a slight decrease of the t-factor, which should favor an increase of tilts and rotations for the SnO_6 octahedra, a decrease of T_C for doped samples is found. The doped samples show a paramagnetic behavior between 5 and 320 K, and the calculated effective paramagnetic moments agree with the spin-only values of the respective magnetic M^{3+} cations used as dopants.

The occurrence of well-developed remanent hysteresis loops confirms the intrinsic ferroelectricity of all samples at room temperature. However, the doped compounds exhibit a considerably larger switching coercive field than $Sr_3Sn_2O_7$, which hinders further the functionality of these new HIFs. The relative dielectric permittivity measurements revealed that this aliovalent cooping strategy is detrimental for the ferroelectric ordering, evidenced by a significant decrease in the T_C for the doped samples together with a strong smoothing of the ferroelectric transition. As t-factor is slightly smaller for the doped samples, this weakening of the ferroelectric order must be attributed to the compositional disorder due to the double aliovalent substitution that introduces a strong disarray in the internal electric field of the samples, making long-range order of the electric dipoles more difficult. This result should be taken into account for the development of future strategies to obtain new multiferroic materials based on the improper hybrid mechanism.

Declaration of Competing Interest

The authors declare the following financial interests/personal relationships which may be considered as potential competing interests:

Data availability

Data will be made available on request.

Acknowledgements

Author contributions

The manuscript was written through contributions of all authors and they have given approval to this final version.

Appendix A. Supporting information

Supplementary data associated with this article can be found in the online version at doi:10.1016/j.jallcom.2024.176148.

References

[1] N.A. Spaldin, R. Ramesh, Advances in magnetoelectric multiferroics, Nat. Mat. 18 (2019) 203–212, https://doi.org/10.1038/s41563-018-0275-2.

[2] R. Gupta, R.K. Kotnala, A review on current status and mechanisms of room-temperature magnetoelectric coupling in multiferroics for device applications, J. Mater. Sci. 57 (2022) 12710–12737, https://doi.org/10.1007/s10853-022-07377-4.

[3] Sh Dong, J. Zhai, J.F. Li, D. Viehland, S. Priya, Multimodal system for harvesting magnetic and mechanical energy, Appl. Phys. Lett. 93 (2008) 103511, https://doi.org/10.1063/1.2982099.

[4] N.A. Hill, Why are there so few magnetic ferroelectrics? J. Phys. Chem. B 104 (2000) 6694–6709, https://doi.org/10.1021/jp000114x.

[5] J. Blasco, V. Cuartero, S. Lafuerza, J.L. García-Muñoz, F. Fauth, G. Subías, Three charge-ordered phases in bilayered $Pr(Sr_{0.1}Ca_{0.9})_2Mn_2O_7$: from antiferrodistortive to ferrodistortive structures, Phys. Rev. B 109 (2024) 024111, https://doi.org/10.1103/PhysRevB.109.024111.

[6] M. Morin, A. Scaramucci, M. Bartkowiak, E. Pomjakushina, G. Deng, D. Sheptyakov, L. Keller, J. Rodriguez-Carvajal, N.A. Spaldin, M. Kenzelmann, K. Conder, M. Medarde, Incommensurate magnetic structure, Fe/Cu chemical disorder, and magnetic interactions in the high-temperature multiferroic $YBaCuFeO_5$, Phys. Rev. B 91 (2015) 064408, https://doi.org/10.1103/PhysRevB.91.064408.

[7] J. Blasco, J.L. García-Muñoz, J. García, G. Subías, J. Stankiewicz, J.A. Rodríguez-Velamazán, C. Ritter, Magnetic order and magnetoelectric properties of R_2CoMnO_6 perovskites (R=Ho, Tm, Yb, and Lu), Phys. Rev. B 96 (2017) 024409, https://doi.org/10.1103/PhysRevB.96.024409.

[8] N.A. Benedek, J.M. Rondinelli, H. Djani, P. Ghosez, P. Lightfoot, Understanding ferroelectricity in layered perovskites: new ideas and insights from theory and experiments, Dalton Trans. 44 (2015) 10543–10558, https://doi.org/10.1039/C5DT00010F.

[9] N.A. Benedek, C.J. Fennie, Hybrid improper ferroelectricity: a mechanism for controllable polarization-magnetization coupling, Phys. Rev. Lett. 106 (2011) 107204, https://doi.org/10.1103/PhysRevLett.106.107204.

[10] I. Etxeberria, J.M. Pérez-Mato, P. Boullay, The role of trilinear couplings in the phase transitions of aurivillius compounds, Ferroelectrics 401 (2010) 17–23, https://doi.org/10.1080/00150191003670325.

[11] Y. Wang, F.-T. Huang, X. Luo, B. Gao, S.-W. Cheong, The first room-temperature ferroelectric Sn insulator and its polarization switching kinetics, Adv. Mater. 29 (2017) 1601288, https://doi.org/10.1002/adma.201601288.

[12] J.J. Lu, X.Q. Liu, X. Ma, M.S. Fu, A. Yuan, Y.J. Wu, X.M. Chen, Crystal structures, dielectric properties, and phase transition in hybrid improper ferroelectric Sr3Sn2O7-based ceramics, J. Appl. Phys. 125 (2019) 044101, https://doi.org/10.1063/1.5051190.

[13] X. Xu, Y. Wang, F.-T. Huang, K. Du, E.A. Nowadnick, S.-W. Cheong, Highly tunable ferroelectricity in hybrid improper ferroelectric $Sr_3Sn_2O_7$, Adv. Funct. Mater. 30 (2020) 2003623, https://doi.org/10.1002/adfm.202003623.

[14] B.H. Chen, T.L. Sun, X.Q. Liu, X.L. Zhu, H. Tian, X.M. Chen, Enhanced hybrid improper ferroelectricity in $Sr_{3-x}Ba_xSn_2O_7$ ceramics with a Ruddlesden–Popper (R–P) structure, Appl. Phys. Lett. 116 (2020) 042903, https://doi.org/10.1063/1.5138672.

[15] X. Sun, Z. Tang, X. Yang, Z. Gao, Y. Wu, J. Jiang, Z. Zhang, S. Jiao, D. Li, H.-L. Cai, X.S. Wu, Structural evolution and phase transition of $Sr_3Sn_2O_7$ doped with Ca, Chem. Phys. Lett. 766 (2021) 138319, https://doi.org/10.1016/j.cplett.2021.138319.

[16] Z.Z. Hu, J.J. Lu, B.H. Chen, X.Q. Liu, X.M. Chen, Improved ferroelectric properties in hybrid improper ferroelectric $Sr_{3-x}Ba_xZr_2O_7$, J. Alloy. Compd. 866 (2021) 158705, https://doi.org/10.1016/j.jallcom.2021.158705.

[17] S. Yoshida, H. Akamatsu, R. Tsuji, O. Hernandez, H. Padmanabhan, A.S. Gupta, A. S. Gibbs, K. Mibu, S. Murai, J.M. Rondinelli, V. Gopalan, K. Tanaka, K. Fujita, Hybrid improper ferroelectricity in $(Sr,Ca)_3Sn_2O_7$ and beyond: universal relationship between ferroelectric transition temperature and tolerance factor in n = 2 Ruddlesden−Popper phases, J. Am. Chem. Soc. 140 (2018) 15690, https://doi.org/10.1021/jacs.8b07998.

[18] D. Chen, H. Wu, W. Cai, C. Zhou, R. Gao, X. Deng, G. Chen, Z. Wang, X. Lei, C. Fu, Superior hybrid improper ferroelectricity and enhanced ferromagnetism of $Ca_3(Ti_{1-x}Co_x)_2O_7$ ceramics through the superexchange interaction, Ceram. Int. 48 (2022) 36358, https://doi.org/10.1016/j.ceramint.2022.08.195.

[19] H. Wu, W. Cai, Z. Liu, D. Chen, R. Gao, G. Chen, X. Deng, Z. Wang, X. Lei, C. Fu, Optimized hybrid improper ferroelectricity of $(Ca_{1-x}Nd_x)_3Ti_2O_7$ ceramics based on soft doping effects, Ceram. Int. 50 (2024) 6845, https://doi.org/10.1016/j.ceramint.2023.12.029.

[20] J. Rodríguez-Carvajal, Recent advances in magnetic structure determination by neutron powder diffraction, Phys. B 192 (1993) 55–69, https://doi.org/10.1016/0921-4526(93)90108-I.

[21] K. Momma, F. Izumi, VESTA3 for three-dimensional visualization of crystal, volumetric and morphology data, J. Appl. Crystallogr. 44 (2011) 1272, https://doi.org/10.1107/S0021889811038970.

[22] O. Mathon, A. Beteva, J. Borrel, D. Bugnazet, S. Gatla, R. Hino, I. Kantor, T. Mairs, M. Munoz, S. Pasternak, F. Perrin, S. Pascarelli, The time-resolved and extreme conditions XAS (TEXAS) facility at the European Synchrotron Radiation Facility: the general-purpose EXAFS bending-magnet beamline BM23, J. Synchrotron Radiat. 22 (2015) 1548, https://doi.org/10.1107/S1600577515017786.

[23] B. Ravel, M. Newville, ATHENA, ARTEMIS, HEPHAESTUS: data analysis for X-ray absorption spectroscopy using IFEFFIT, J. Synchrotron Radiat. 12 (2005) 537, https://doi.org/10.1107/S0909049505012719.

[24] U. Chowdhury, S. Goswami, D. Bhattacharya, A. Midya, P. Mandal, Determination of intrinsic ferroelectric polarization in lossy improper ferroelectric systems, Appl. Phys. Lett. 109 (2016) 092902, https://doi.org/10.1063/1.4961988.

[25] A.J. Joseph, B. Kumar, Study of true-remanent polarization using remanent hysteresis task and resistive leakage analysis in ferroelectric $0.64Pb(Mg_{1/3}Nb_{2/3})O_3$-$0.36PbTiO_3$ ceramics, Sol. State Comm. 271 (2018) 11–15, https://doi.org/10.1016/j.ssc.2017.12.017.

[26] R.D. Shannon, Revised effective ionic radii and systematic studies of interatomie distances in halides and chaleogenides, Acta Cryst. A 23 (1976) 751–767, https://doi.org/10.1107/S0567739476001551.

[27] G. Subías, J. García, M.G. Proietti, J. Blasco, X-ray-absorption near-edge spectroscopy and circular magnetic x-ray dichroism at the Mn K edge of magnetoresistive manganites, Phys. Rev. B 56 (1997) 8183, https://doi.org/10.1103/PhysRevB.56.8183.

[28] C. Booth, F. Bridges, G.H. Kwei, J.M. Lawrence, A.L. Cornelius, J.J. Neumeier, Lattice effects in $La_{1-x}Ca_xMnO_3$ (x= 0→1): relationships between distortions, charge distribution, and magnetism, Phys. Rev. B 57 (1998) 10440, https://doi.org/10.1103/PhysRevB.57.10440.

[29] M.C. Sánchez, G. Subías, J. García, J. Blasco, Stability of the tetragonal $Mn^{3+}O_6$ distortions in the $LaMn_{1-x}Ga_xO_3$ series by x-ray absorption spectroscopy, Phys. Rev. B 69 (2004) 184415, https://doi.org/10.1103/PhysRevB.69.184415.

[30] Y. Zhang, J. Wang, P. Ghosez, Unraveling the suppression of oxygen octahedral rotations in $A_3B_2O_7$ Ruddlesden-Popper compounds: engineering multiferroicity and beyond, Phys. Rev. Lett. 125 (2020) 15761, https://doi.org/10.1103/PhysRevLett.125.157601.

[31] W. Yi, T. Kawasaki, Y. Zhang, H. Akamatsu, R. Ota, S. Torii, K. Fujita, $La_2SrSc_2O_7$: a-site cation disorder induces ferroelectricity in ruddlesden-popper layered perovskite oxide, J. Am. Chem. Soc. 146 (2024) 4570, https://doi.org/10.1021/jacs.3c11546.

[32] G.A. Bain, and J. F. Barry. Diamagnetic corrections and Pascal's constants, J. Chem. Educ. 85 (2008) 532, https://doi.org/10.1021/ed085p532.

[33] J.B. Goodenough, An interpretation of the magnetic properties of the perovskite-type mixed crystals $La_{1-x}Sr_xCoO_{3-\lambda}$, J. Phys. Chem. Solids 6 (1958) 287, https://doi.org/10.1016/0022-3697(58)90107-0.

[34] J. Kanamori, Superexchange interaction and symmetry properties of electron orbitals, J. Phys. Chem. Solids 10 (1959) 87, https://doi.org/10.1016/0022-3697(59)90061-7.

[35] J. Blasco, J. García, J. Campo, M.C. Sánchez, G. Subías, Neutron diffraction study and magnetic properties of $LaMn_{1-x}Ga_xO_3$, Phys. Rev. B 66 (2002) 174431, https://doi.org/10.1103/PhysRevB.66.174431.

[36] J.B. Goodenough, R.I. Dass, J. Zhou, Spin-glass to ferromagnet transition in $LaMn_{1-x}Sc_xO_3$, Sol. State Sci. 4 (2002) 297, https://doi.org/10.1016/S1293-2558(01)01255-9.

[37] R. Zhang, J.Fang Li, D. Viehland, Effect of aliovalent substituents on the ferroelectric properties of modified barium titanate ceramics - relaxor ferroelectric behavior, J. Am. Ceram. Soc. 87 (2004) 864–870, https://doi.org/10.1111/j.1551-2916.2004.00864.x.